70th International Astronautical Congress (IAC), Washington D.C., U.S.A., 21-25 October 2019.


IAC–19–B4.8.10

# Capabilities of a Nano-LIDAR for Future Reconnaissance Missions to NEOs

**Lewis Walker[a], Massimiliano Vasile[a]**

[a]*Department of Mechanical & Aerospace Engineering,University of Strathclyde, James Weir Building, 75 Montrose Street, Glasgow, United Kingdom G11XJ*, lewis.walker@strath.ac.uk, massimiliano.vasile@strath.ac.uk

**Abstract**

In this paper we estimate by numerical modelling the maximum range capability of a CubeSat-borne laser rangefinder in fast asteroid flyby scenarios requiring high single pulse detection probabilities. The model is based around detected photon counts in a pair of Geiger mode avalanche photodiodes (GM-APDs). Simulated datasets for fast flybys are generated by the model to assess performance. The model is also modified to assess the feasibility of performing radioscience measurements to determine asteroid mass, by measuring trajectory deflections on the order of $\mu ms^{-1}$ during a dual-spacecraft flyby. Similar datasets are generated by the model and filtered to simulate radioscience measurements. It was found that limits of detectability of the relative velocity using this method are on the order of $10\mu ms^{-1}$

**Keywords:** Asteroid flyby, Formation flying, Nanosatellite, LIDAR

## 1. Introduction

As of January 2019, there have been 19381 near-earth asteroids (NEAs) discovered by astronomers and space agencies worldwide [1]. Of these, 1957 are considered to be 'potentially hazardous asteroids' (PHAs) - asteroids whose minimum orbit intersection distance with Earth is less than 0.05AU, and pose a potential collision risk. 156 of these identified PHAs have diameters larger than 1km. These numbers grow every year at an increasing rate as more are discovered with improving telescope technologies. A limitation of Earth or LEO based observations of these asteroids is that due to extremely long distances and limited observation windows - many objects NEAs having only been observed once or twice - we are left with with relatively large uncertainties on their orbital elements, and little to no further information on them with regard to composition, structure and mass.

Only a handful of missions to date have ever come close to asteroids or comets, to explore at a close range, such as Hayabusa, Near Shoemaker, Rosetta, Deep Impact, and Deep Space 1. These missions cost in the hundreds of millions of US dollars each. Given the large number of NEAs, it is obviously infeasible to visit a significant portion of them at close range using similar mission frameworks. However, the rise of CubeSat and nano-satellite technology presents a low-cost, scalable option for asteroid reconnaissance. Recently, the first ever CubeSats deployed in an interplanetary mission, MarCO-A and MarCO-B, successfully completed their mission of providing a communications relay to Earth for the InSight lander during EDL. This demonstrates CubeSats are a viable option for deep space missions. Other deep-space CubeSat missions are planned such as NEA-Scout [2], and many others proposed such as DISCUS [3], and NEACORE [4] which all aim to explore the NEA population

A framework for low-cost, large-scale asteroid exploration was proposed in 2019 [4] in which pairs of CubeSats would perform tandem close flybys of a series of NEAs. Satellite pairs could feasibly visit in the region of 5 NEAs each - and in a single dedicated launch anywhere from 6-100 pairs could be deployed, which would vastly increase the visited fraction of the NEA population.

In this paper we estimate the maximum reliable operational range for a CubeSat-scale laser rangefinder in such asteroid reconnaissance missions for direct ranging of the target asteroid, and assess the feasibility of using LIDAR for intersatellite ranging (ISR) to detect relative drifts to precision levels of $\mu$m/s, in order to characterize the mass of the

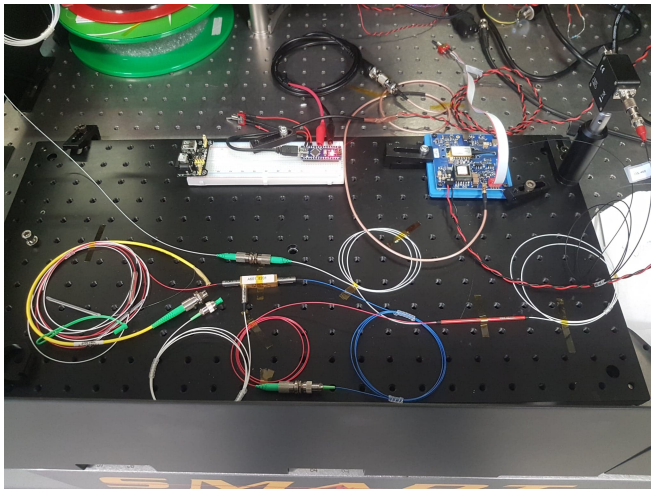

Fig. 1: Benchtop prototype of laser pulse amplifier (in progress)

target asteroid. The pulsed laser source for such a LIDAR system is in development at the University of Strathclyde, and an early benchtop prototype can be seen in Figure 1.

The results of this work inform some of the specifications for the prototype, mainly the requirement on the pulse energy.

## 2. Mission Scenario

The mission scenario being considered as the context for this paper is as follows, and is the same as proposed previously in [4]. Pairs of identical CubeSats, each carrying a LIDAR and a camera, perform a series of asteroid flybys in formation, flying by on opposite sides of the target objects. NEACORE is a low-cost large scale NEA exploration framework, and the goal is to recover as much scientific information on as many targets as possible for minimum cost. Primary objective is improvement of the targets' emphemeris, secondarily to characterize mass and resolve surface features and physical structure including shape and size. The latter two are done with the camera, and the former two goals can be achieved by the LIDAR, by direct ranging of the asteroid during flyby and measurement of the relative state of the two satellites before and after passing through the targets' gravity fields. Object ephemeris is improved by measuring the position and velocity of the target relative to the satellite during flyby.

## 3. Instrument Design Considerations

### *3.1 Laser System*

The primary aim of laser system design in order to maximise LRF range capability is the maximisation of pulse energy while minimizing size, weight and power (SWaP). Waste heat must also be minimized if the device is intended for extended operation as nanosatellites typically will not be able to have large active cooling systems. All-fiber laser systems are rather attractive for space applications as they are much less sensitive to launch vibrations due to a lack of free-space beams requiring precisely aligned components. Their active media can be tightly coiled into a small volume, allowing for extremely long active fiber lengths and hence extremely high optical gain. They can also produce higher quality, low divergence beams as single-mode fiber can be used, which is particularly important for very distant targets.

SWaP restrictions immediately rule out actively q-switched fiber devices as the EOMs used require voltages in the kV range, which is unrealistic on a nanosatellite. AOMs are still fairly power-hungry and introduce losses in their deflection efficiency, tend to be fairly bulky relative to available volume in a CubeSat and generate waste heat which must be dissipated.

Fiber pulse amplifiers on the other hand offer the possibility of energetic pulses with adjustability in repetition rate, simple systems with low part numbers and masses, thermals that are localized and easy to control, and mostly passive components other than the seed and pump laser diodes. These systems take the fiber-coupled output of a pulsed laser diode, and pass this through one or several amplification stages each consisting of a section of rare-earth doped fiber, and filtering out amplified spontaneous emission (ASE) between each stage. Simple, compact, all-fiber pulse amplifiers can achieve pulse energies on the order of millijoules which is desirable in this application.

Additionally, a prototype pulse source for this application is being constructed at the University of Strathclyde to demonstrate the feasibility of achieving CubeSat-level SWaP while still generating pulse energies high enough to be useful in this application.

### *3.2 Collector*

A circular collection aperture of 8cm diameter is assumed in the model, which would comfortably fit in a single CubeSat unit. The collected light would be focussed down into a fiber coupler, then travel in-fiber to the detectors.

*3.3 Detector*

Due to the low number of returning photons at extremely long ranges combined with the low level of noise light in space, single photon sensitive detectors would be well-suited for this application. A typical single photon detector consists of a single single-photon avalanche photodiode (SPAD) pixel or array of pixels. The pixels are reverse-biased beyond their breakdown voltage, such that any single ionization event within a pixel - from an incoming photon or dark count - causes a self sustaining avalanche of carrier generation within that pixel. This causes a detectable current from the triggered pixel, which can be read out to determine if a photon or dark count has arrived during the measurement time. This avalanche is stopped by lowering the bias voltage below the breakdown voltage, which occurs at the end of each temporal measurement window, or range gate. At the end of each range gate, the number and location of pixels triggered in that gate is read out, pixels are reset, and the sensor is then ready for the voltage to be raised again and the next range gate to begin. Number of triggers per time bin can be plotted and used to detect a returning laser pulse by a spike in the histogram. The time since the pulse was sent out is then compared with the return pulse arrival time to determine the time of flight (ToF) and distance to the target.

For long and unknown ranges to the target, the range gating approach introduces some problems. Firstly, the maximum gate length is finite - limited by noise and dark counts which gradually trigger more and more pixels until the array in unresponsive to signal. This means gates cannot be made arbitrarily long and simply reset upon detecting a return pulse. Additionally, significant dead time during the reset period between range gates exists, during which the return pulse could easily land and go undetected. Thus a continuous, arbitrary length gate is desirable.

To address this, an instrument with two parallel detector arrays was modelled. The signal would be split equally across two detectors which would have temporally overlapping range gates, both synchronized with respect to a master clock for timing, which is reset every time a pulse is launched. Thus there is a net zero dead time, as at least one of the detectors is always sensitive to incoming photons.

## 4. Detector Modelling Technique

*4.1 Asteroid Ranging*

*Collected Photon Rate*

Luo et. al [5] modelled the rate of primary electron generation in a (SPAD) based detector to assess performance limitations, which forms the initial basis for this work. The initial derivation follows closely to that of Luo, and the rate of primary electron generation per pixel due to signal photons as a function of time was derived to be

$$S_{PE}(t) = \frac{\eta_q \eta_t \eta_r \alpha F_{fill} F_{ref} F_{col}}{h\nu n_{px}} P_{emit}(t - \frac{2R}{c}) \quad (1)$$

Where $\eta_q$ is the detector quantum efficiency, $\eta_t$ and $\eta_r$ are the optical transmission and receiving efficiencies, $\alpha$ is the target albedo, $F_{fill}$, $F_{ref}$ and $F_{col}$ are respectively the SPAD array fill factor (including microlens array fill factor), the fraction of outgoing light that hits the target object, and fraction of reflected light that is collected, $h\nu$ is the photon energy and $n_{px}$ is the number of pixels in the modelled array. $P_{emit}(t)$ is the emitted laser power as a function of time (modelled to have a temporally square profile with pulsewidth 3ns, amplitude scaled to the pulse energy), $R$ the range to target and $c$ the speed of light. $\alpha = 0.2$ is assumed for asteroid targets and $\alpha = 0.8$ for ISR simulations.

Due to beam divergence, the beam area at the target will be much larger than it was when the pulse was fired, with divergence half angle equal of $\theta = M^2 \frac{\lambda}{\pi w_0}$. The target is assumed to reflect isotropically across a hemisphere with radius equal to the range from target to satellite. $F_{ref}$ and $F_{col}$ hence are defined as follows

$$F_{ref} = min(1, \frac{A_{ast}}{A_{beam}}) \quad (2)$$

$$F_{col} = min(1, \frac{A_{col}}{2\pi R}) \quad (3)$$

The total rate of primary electron generation per pixel is

$$T_{PE}(t) = \frac{1}{2}(S_{PE}(t) + N_{PE}(t)) + DCR \quad (4)$$

Where $N_{PE}(t)$ is the noise PE generation rate, derived similary to the above and accounting for both direct solar photons and solar photons reflected from the target, DCR is the per-pixel dark count rate, and the factor or $\frac{1}{2}$ is due to the signal being split over two identical SPAD arrays as previously mentioned.

Photon counting is a probabilistic process and follows Poisson statistics. As in Luo [1], the probability of detecting k photons in a given time window is given by

$$P(k) = \frac{K_{av}^k}{k!} exp(-K_{av}) \quad (5)$$

Where $K_{av}$ is the average number of photons expected in the time window. Setting k = 0 gives the no-trigger probability for a given time bin, and $1 - P_{notrigger}$ is the probability that the pixel will trigger. Thus, assuming $T_{PE}(t)$ is constant across one time bin,

$$P_{trigger} = 1 - exp(-T_{PE}(t)t_{bin}) \quad (6)$$

Where $t_{bin}$ is the duration of one time bin (set to 200ps in this model). The probability for that pixel having NOT triggered in all previous time bins since the beginning of the range gate is

$$P_{untriggered} = \prod_{i}^{i-1} exp(-T_{PE}(t_i)t_{bin}) \quad (7)$$

where $t_i$ is the start time of each time bin relative to the gate start time, and summing over $i$ sums over all previous time bins. Thus the final probability for a pixel to trigger in a given time bin is

$$P_{trigger} = (1-exp(-T_{PE}(t)t_{bin})) \prod_{i}^{i-1} exp(-T_{PE}(t_i)t_{bin}) \quad (8)$$

Per-pixel trigger probabilities are multiplied by $n_{px}$ to determine the mean number of pixels triggered in each time bin, which is then used as the mean of a Poisson distribution to generate a random number which is the actual number of triggers in that time bin. A histogram is plotted, giving a simulated measurement of a returning laser pulse. An example measurement histogram can be seen below. The data is smoothed by conversion to a rolling average across $\pm t_{pulse}/2$ in order to improve the curve fitting for spike detection.

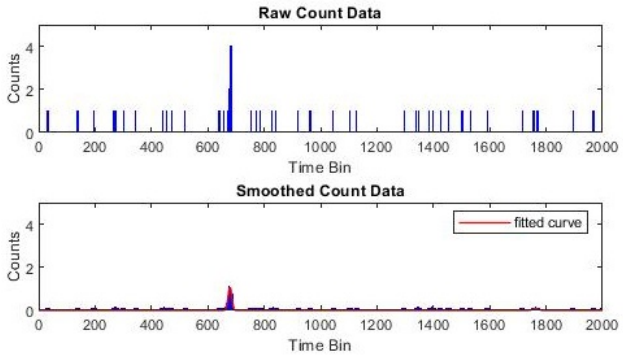


Fig. 2: *Simulated measurement of a single range gate with fitted Gaussian curve*

*Noise Sources*

A number of noise sources were included in the model to more realistically simulate measurements. Dark Count Rate (DCR) was modelled as 50kHz per pixel. This is likely a pessimistic estimate, as DCR if InGaAs SPADs varies widely in the literature [6][7] and is also temperature dependent, and it is unclear what detector cooling capabilities would be possible on a CubeSat platform for such an instrument at this time. Itzler [7] characterized a 32 x 32 InGaAs SPAD array similar to as is modelled in this paper, and all pixels had a DCR of less than 50kHz. This is a reasonable estimate for initial performance modelling.

Background signal-wavelength photons from the Sun were included as an additional noise source. Solar flux at the signal wavelength of 1064nm is $0.647Wm^{-2}nm-1$ at 1AU, which is where the measurements are assumed to be taken [8]. A bandpass filter in the optical path of $\pm 2.5nm$ around the signal wavelength was assumed. The worst case scenario for sunlight noise was modelled, with the collector being exposed to normally incident sunlight.

Solar photons reflected from the target object and impinging on the collector were also accounted for. Full illumination of the target with sunlight was also assumed for the worst case.

In asteroid ranging, for each pulse a surface slope angle was randomly generated between 0 and 60 degrees which spreads the pulse shape temporally. Since the range is detected by centroid of a fitted Gaussian curve, this will introduce noise in the detected range.

*Detection Criteria*

A simple algorithm was developed to detect spikes in the produced histograms. A 4-term Gaussian was fitted for each, and the one with the highest amplitude was selected as the 'detection' for that simulation. A minimum threshold must be set for the amplitude of the fitted curve to be considered a signal spike and not a noise fluctuation. This was derived by observing the behaviour of the model when only background counts were considered. 500 dark runs ($E_{pulse} = 0$) of the model were simulated to determine the distribution of fitted spike amplitude, and a value of 5 standard deviations above the mean was used as the threshold for the fit to be considered a true detection in later simulations.

### *4.2 Model Modifications for Inter-satellite Ranging*

In intersatellite ranging (ISR), a two-way ranging approach is assumed, where both satellites would carry identical LIDARs which would each point at the other spacecraft. When satellite A fires a pulse, it is detected by satellite B, which in turn fires a response pulse back at satellite A. This results in a stronger detected pulse at satellite A, thus this technique be employed at longer ranges than if simple scattering of the primary pulse was used to detect range.

The rate of signal PE generation is defined similarly to in the asteroid case, with the removal of the factor $F_{ref}$, and $F_{col}$ is no longer defined as a fraction of a hemisphere, but as a fraction of the beam area collected by satellite A, fired by satellite B. Additional time delay factors, $t_{response}$ and $t_{jitter}$ should also be added, such that $P_{emit}(t) = P_{emit}(t - \frac{2R}{c} - t_{response} - t_{jitter})$. $t_{response}$ must later be compensated when recovering the detected range from the centroid of the fitted curve. $t_{jitter}$ is a noise term due to variations in $t_{response}$ which is generated for each simulation and added to the return signal delay. $t_{jitter}$ is a normal randomly generated time offset with $\mu = 0s$ and $\sigma = 0.1ns$.

Beam divergence is assumed to be significantly larger than in the asteroid case in order to reduce the pointing accuracy requirement on the LIDAR due to the small angular size of a spacecraft compared with an asteroid, and reduce the likelihood of the spacecraft drifting out of each other's laser beams. Divergence half-angle was set at 50mrad for ISR, which results in a 10km spot diameter at 100km range.

Due to the incredibly sensitive nature of single photon counting detectors, it was found that for the two-way ranging approach, even with R = 100km and high beam divergence, very low pulse energies on the order of $1\mu J$ are sufficient to be detected. A $1\mu J$ pulse at 1064nm consists 5.4x$10^{12}$ photons - spread over a 10km circular spot, there are 6.8x$10^{4}$ photons $m^{-2}$, and approximately 350 impinge on the 8cm diameter circular aperture. Since a hugely overpowered laser for this application would already be on board the spacecraft if it were capable of asteroid ranging at similar distances, it can be assumed that any practical limit on range for ISR via the two-way ranging method is well beyond the actual ranges that are in question, which are on the order of 100km.

## 5. Range Limit Results

### *5.1 Spike Intensity Threshold for Detection*

As described in 4.1.3, a distribution of dark fits was obtained from 500 simulations with $E_{pulse} = 0$. The distribution had a mean value of 0.1582 with standard deviation 0.0202. Thus a value of $\mu + 5\sigma = 0.2591$ was used as a threshold for fitted spike amplitude to be considered a detection of a returning pulse. This applies for both asteroid ranging and ISR measurement scenarios.

### *5.2 Asteroid Ranging in Fast Flybys*

In the given mission scenario of a fast asteroid flyby, we have a one-time measurement window with rapidly changing range and angular position. This necessitates a high detection probability for each individual pulse, as techniques such as range gate summation cannot be applied to increase SNR above an acceptable level.

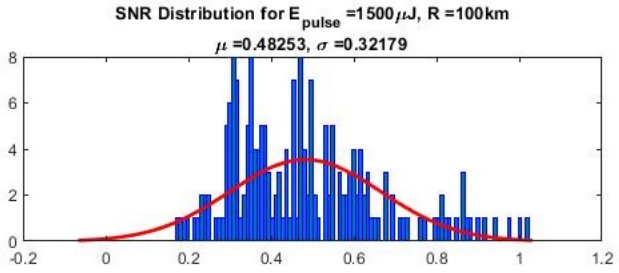


Fig. 3: Example of a typical SNR distribution

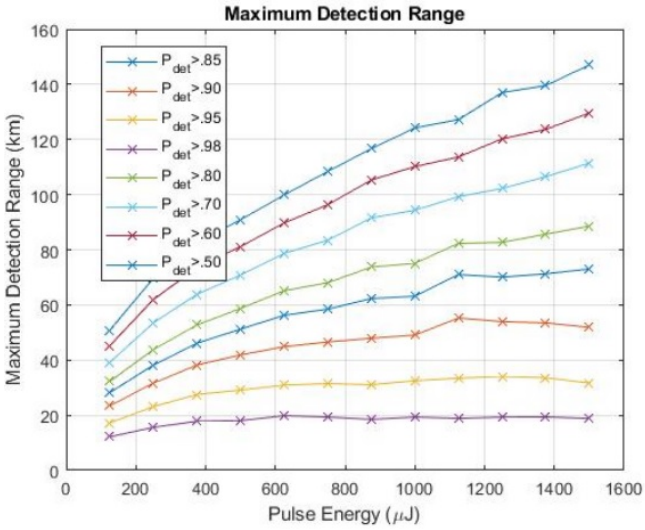


Fig. 4: Maximum Operational Range of a LIDAR for Asteroid Measurements

200 pulses were simulated for a number of pairings of $R$ and $E_{pulse}$. Spike amplitude for each pairing was found to follow an approximately normal distribution, so a curve was fitted and used to determine the probability of a given pulse to fall above the threshold amplitude determined in 5.1. An example of this can be seen in Figure 3.

Holding $E_{pulse}$ constant and plotting the detection probability $P_{det}$ as a function of range allows the approximation of the maximum operational range of a LIDAR with a given pulse energy, if a minimum threshold is set on $P_{det}$. This detection probability is somewhat arbitrary and dependent on the exact parameters of the flyby being considered, so results were plotted for various values of $P_{det}$ in Figure 4.

It can be seen from these results that the maximum reasonable range to expect a LIDAR to operate reliably is in the region of 30-50km from the target. This follows the curves

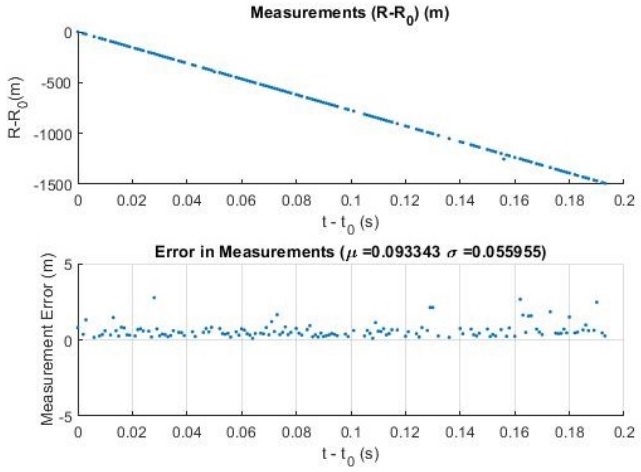


Fig. 5: Simulated measurements and errors during fast asteroid flyby at 8km, $E_p = 500\mu J$

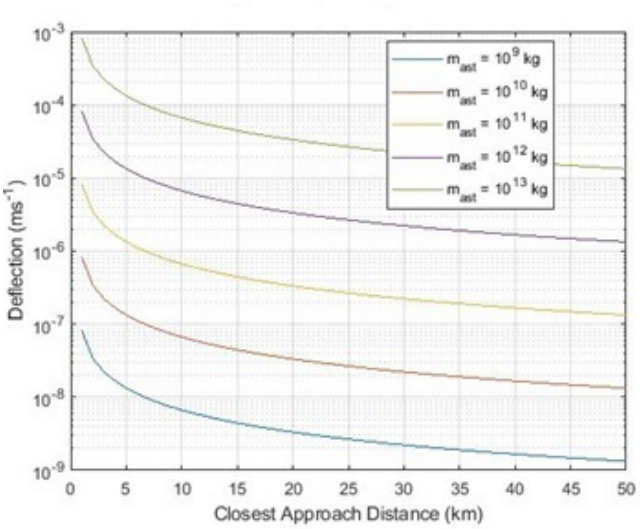


Fig. 6: Deflection as a function of m˙ast and flyby distance

of a $90 - 95\%$ pulse detection probability, at the upper end of the range of pulse energies simulated. During a fast flyby of 8km/s, with 20km closest approach and a 400m diameter asteroid, measuring at 45 degrees to the closest approach vector, with a sample rate of 1kHz, there is time for approximately 70 samples as the asteroid passes through the path of the pulse train. Even missing 10% of these would still allow for the reconstruction of the line-of-sight velocity which is the desired parameter for improving the ephemeris of the object. If even a single pulse were successfully detected, the position of the object would be recoverable from this alone. Figure 5 shows the simulated LIDAR results from such a flyby as previously mentioned, at various pulse energies. Even in cases with lower pulse energy and some missing samples, the slope is clearly recoverable. Additionally, if one assumes that all or almost all pulses that hit the asteroid are detected, one can recover the size of the object in the direction of the beam path across the surface. Typical error range for asteroid ranging measurements was in the $<$1m range. This is more than sufficient as-is for this application, as the position of the satellite relative to the Sun is not known nearly as precisely as this, so further filtering to improve the relative state would not be beneficial.

## 6. Radioscience Modelling

If two identical spacecraft can be arranged to fly by an asteroid on opposing sides, their relative velocities will be affected slightly by the gravity of the object. If this trajectory deflection could be measured, the approximate mass of the object could be inferred. Figure 7 shows the deflection from the unaffected trajectory when flying by various mass NEAs at 40km, in order to give an order of magnitude for this measurement. Additionally, figure 6 shows the deflection as a function of flyby distance and asteroid mass.

It can be seen from Figures 7 and 6 that deflections on the order of $1 - 10\mu$m/s are possible depending on the asteroid mass, flyby velocity and altitude. This is significantly less than the noise fluctuations in the measurements, which are on the order of 1-10cm. In order to reduce the noise level and improve the knowledge of the relative state of a pair of satellites in a short measurement window, Kalman filtering was applied.

Since this LIDAR only directly measures the range to target, the relative velocity is a quantity derived from measurements. Line of sight velocity was calculated on the fly as new state estimates are made, as in Equation 9.

$$v_i = \frac{x_i - r_{i-1}}{dt} \tag{9}$$

where $r_i$ and $v_i$ are the range and line-of-sight velocity measurements, and $x_i$ are the on-axis components of each state estimate.

Simulated datasets were generated using the LIDAR model described in Section 4, with modifications to make the model suitable for ISR by TWR (Section 4.2). Relative velocity was set to have the two satellites drift together at various sub-mm/s rates at a range of 80km with a laser pulse energy of $1\mu J$ and sample periods between 5s and 60s, for 1000 samples. Sample rate in this scenario cannot be increased to reduce convergence time, as the relatively large fluctuations in consecutive samples of $v_{los}$ with a very small $dt$ result in wildly variable measurements of instanta-

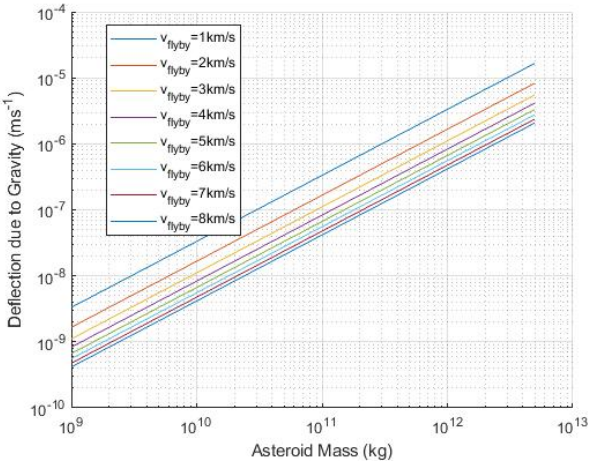


Fig. 7: Trajectory deflection flying by asteroids of at various speeds

| $v_{rel}(\mu ms^{-1})$ | Filter ($\mu ms^{-1}$) | Lin. Reg. ($\mu ms^{-1}$) |
|---|---|---|
| 200 | 197.9 | 199.04 ($R^2$ = 0.9896) |
| 20 | 17.48 | 20.02 ($R^2$ = 0.7158) |
| 2 | -17.53 | 1.1585 ($R^2$ = 0.4188) |

Table 1: $v_{los}$ recovered via filter convergence and linear regression performed directly on filtered range measurements

neous velocity which the filter fails to converge even with very long $dt$ and integration times. A typical filter output can be seen in Figure 8.

Linear regression was also performed on the filter output for position component of the relative state to recover line-of-sight velocity by an alternative means.

It can be seen from Table 1 that reasonably accurate filter convergence was achieved for $v_{rel} = 200\mu ms^{-1}$ and $v_{rel} = 20\mu ms^{-1}$. The filter could not converge on an accurate value for $v_{rel} = 2\mu ms^{-1}$, and instead always converged on a negative drift rate (satellites drifting apart rather than together). Linear regression on the filtered range measurements tended to outperform the filter velocity state output however. Linear regression still produced results accurate to the order of magnitude of the true drift velocity down to the $2\mu ms^{-1}$ level, and with the correct sign unlike the velocity filter. However as the drift velocity dropped below $2\mu ms^{-1}$, a small systematic error in the drift velocity became more and more apparent in comparison with the scale of $v_{los}$, indicating a potential issue with the modelling technique used.

Figures 9 and 10 show how the slope uncertainty in the linear regression technique changes with 1000 samples at

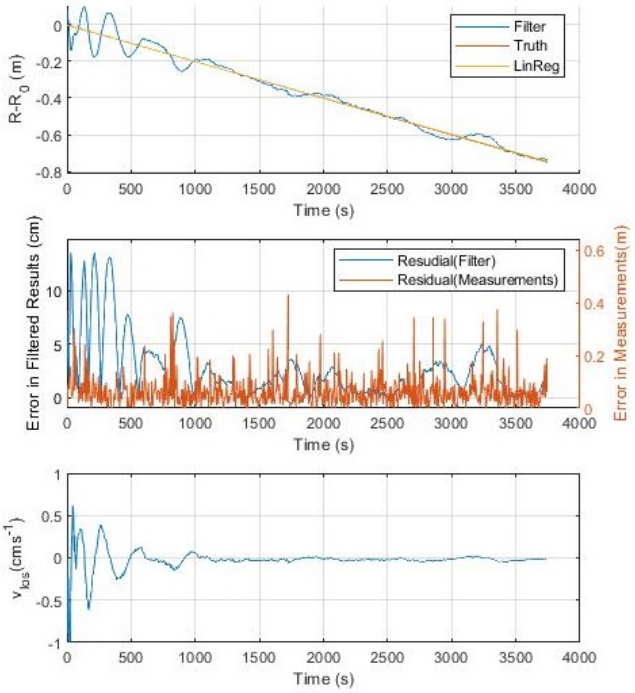


Fig. 8: Typical filter performance, $v_{rel} = 200\mu ms^{-1}, dt = 5s$

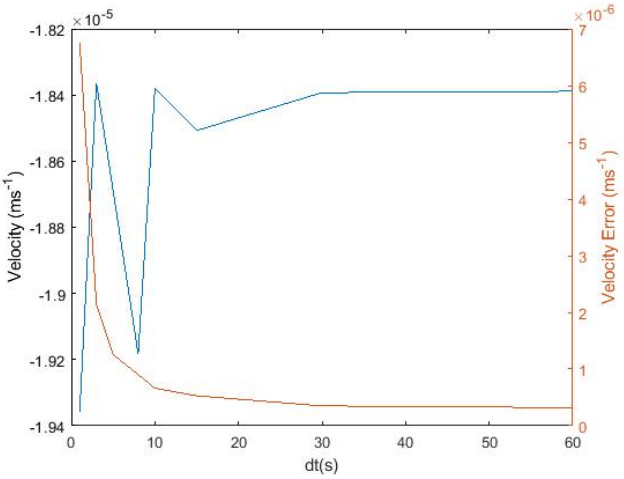


Fig. 9: Measured velocity and uncertainty for $v_{rel}$=20 $\mu ms^{-1}, 1000 samples$

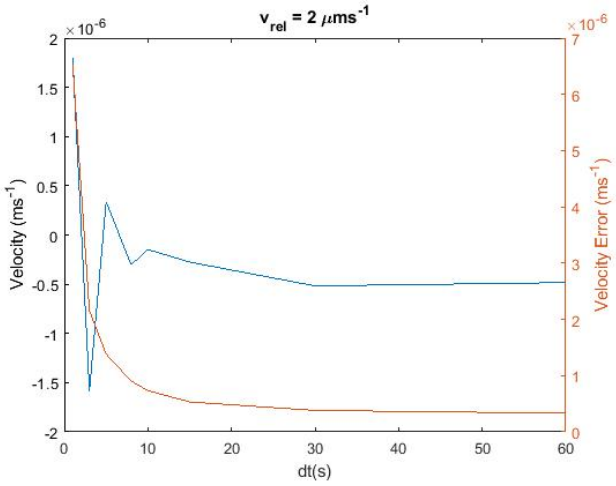


Fig. 10: Measured velocity and uncertainty for $v_{rel}$=2 $\mu ms^{-1}, 1000 samples$

various repetition rates. It can be seen that longer dt results in lower uncertainty in the fit, however there is a systematic underestimation of $1.5\mu ms^{-1}$ relative to the true value, however with longer dt the uncertainty in the linear regression does become less than the magnitude of the velocity.

These results indicate that using these techniques, ISR drift rate measurements could be detected down to the level of tens of microns per second, corresponding to asteroid masses of approximately $10^{11}$ kg on timescales of approximately 1 hour. Numerous other formation flying applications could also be met with such a system, that need not be so overpowered if asteroid ranging is not also required of it.

## 7. Conclusions

As seen in Figure 4, the maximum operational range for a CubeSat borne LIDAR in fast asteroid flybys is highly dependent on the requirement for individual pulse detection probability. $P_{det} = 85\%$ is a very conservative limit for all but the fastest flybys to still allow line-of-sight velocity to be measured, which requires observations to be performed at up to ~60km. Higher $P_{det}$ is desirable if using the LIDAR to measure the asteroid's size along the beam track.

Additionally, it was found that detection of very small line-of-sight relative velocities for two satellites in a tandem asteroid flyby, down to the order of $20\mu ms^{-1}$, can be recovered using the same instrument (by tapping a very small portion of generated pulse energy) as that used for asteroid ranging, and would even work at vastly greater distances due to the higher number of collected photons per pulse. Relative velocity was recovered using two methods, Kalman filtering of instantaneous range rate measurements, and linear regression on the range output of the Kalman filter. The latter tended to outperform the former in the simulations performed, and was able to detect relative velocity down to slightly lower levels than filtering of range rate measurements.

With the exception of SPAD arrays, all technologies required for the instrument proposed are currently available commercially and would not require extensive development. To the author's knowledge, only single pixel SPADs are currently commercially available, however large multipixel arrays have been produced and characterized in the literature, and may become available commercially in the near future.

## References

[1] *JPL Small Body Database*. `https://ssd.jpl.nasa.gov/sbdb.cgi`. Accessed Jan 2019.

[2] Leslie McNutt et al. "Near-earth asteroid (NEA) scout". In: *AIAA Space 2014 Conference and Exposition*. 2014, p. 4435.

[3] Patrick Bambach et al. "DISCUS–The Deep Interior Scanning CubeSat mission to a rubble pile near-Earth asteroid". In: *Advances in Space Research* 62.12 (2018), pp. 3357–3368.

[4] Lewis Walker et al. "Nanospacecraft exploration of asteroids by collision and flyby reconnaissance". In: *Low-Cost Planetary Missions Conference*. 2019.

[5] Hanjun Luo et al. "Maximum detection range limitation of pulse laser radar with Geiger-mode avalanche photodiode array". In: *Journal of Modern Optics* 62.9 (2015), pp. 761–768.

[6] Mark A Itzler et al. "Single photon avalanche diodes (SPADs) for 1.5 $\mu$ m photon counting applications". In: *Journal of Modern Optics* 54.2-3 (2007), pp. 283–304.

[7] Mark A Itzler et al. "Advances in InGaAsP-based avalanche diode single photon detectors". In: *Journal of Modern Optics* 58.3-4 (2011), pp. 174–200.

[8] Xiaoli Sun et al. "Mars 1064 nm spectral radiance measurements determined from the receiver noise response of the Mars Orbiter Laser Altimeter". In: *Applied optics* 45.17 (2006), pp. 3960–3971.